(Received 19 February 2026, Accepted 9 April 2026, Scheduled 25 April 2026)

Edge-Fusion-Based Graph Attention Network for Microwave Breast Tumor Localization

Hongchao Xie[1], Xia Xiao[1,*], Yu Liu[1], and Min Lu[2]

[1]*State Key Laboratory of Advanced Materials for Intelligent Sensing*
Tianjin Key Laboratory of Imaging and Sensing Microelectronic Technology
School of Microelectronics, Tianjin University, Tianjin 300072, China
[2]*School of Automation and Information Engineering, Xi'an University of Technology, Xi'an 710048, China*

ABSTRACT: Objective: To enable the direct joint prediction of tumor center coordinates and radius in non-imaging ultra-wideband (UWB) breast sensing, we propose an edge-fusion-based graph attention framework for learning from multi-channel backscattered signals without the need for image reconstruction. Methods: Breast models were generated using finite-difference time-domain (FDTD) simulations. Backscattered signals were preprocessed using the dual-tree complex wavelet transform (DTCWT). UWB measurement channels were reformulated as a graph, where each transmitter-receiver channel was treated as a node, and edges were defined by shared antennas. Edge features were fused into graph attention message passing to emphasize more tumor-relevant channels, followed by a multi-task regression head to predict tumor center coordinates and radius. Results: Across four breast density categories, mean center localization error (CLE) remained below 2.5 mm, and the mean of comprehensive overlap index (COI), area recall ratio (ARR), and area precision ratio (APR) exceeded 0.50 in all models. These results indicate effective joint localization and size estimation across heterogeneous breast models.

1. INTRODUCTION

Breast cancer remains one of the most common malignancies among women worldwide. Early diagnosis is critical for improving patient prognosis and treatment outcomes [1, 2]. In recent years, both the overall incidence of breast cancer and the proportion of cases in younger populations have increased [3], further driving the demand for safe, convenient, and repeatable screening technologies. Ultra-wideband (UWB) microwave sensing has become a promising noninvasive breast detection method due to its non-ionizing nature, high tissue penetration, and low cost [4]. The physical basis of this technology is the difference in dielectric properties between tumor and normal breast tissue, which leads to the scattering effect of the incident electromagnetic wave. Consequently, tumor-related information can be encoded in the measured backscattered signals and exploited for localization [5].

Since the pioneering work by Hagness et al. [6], microwave breast imaging has mainly followed two technical routes, which are radar-based beamforming and tomography-based inversion of dielectric distributions [7–11]. Tomographic inversion is computationally demanding due to the nonlinearity and ill-posedness of the inverse problem. Meanwhile, detecting small tumor signals remains a considerable challenge because they are often masked by clutter, multipath propagation, and skin reflections interference, all of which inevitably reduce spatial resolution and introduce imaging artifacts.

In recent years, intelligent microwave breast tumor detection has attracted extensive attention and achieved significant progress owing to rapid advances in artificial intelligence. This technology is applied to two categories of problems. One is to improve the image reconstruction process based on traditional imaging methods, such as learning inversion or post-processing, to enhance the reconstruction quality and speed [12, 13]. The second is the use of artificial intelligence methods to directly regress target parameters from measured signals in an end-to-end manner without explicit image reconstruction, thereby achieving tasks such as tumor detection, benign and malignant classification, and tumor localization [14–17]. These methods significantly reduce computational complexity through data-driven feature learning, demonstrating the enormous potential of artificial intelligence in microwave breast tumor localization.

Nevertheless, existing artificial intelligence-based methods still have several limitations. On the one hand, although several studies have been able to estimate tumor location or spatial extent, direct joint prediction of tumor center coordinates and radius within a unified framework remains limited. In practice, tumor location mainly affects wave propagation paths and channel sensitivity, whereas tumor size mainly affects scattering strength and waveform characteristics. Since the backscattered signals are jointly influenced by both factors, evaluating prediction reliability using positional error alone, without considering tumor size, can lead to an incomplete or even misleading assessment. On the other hand, graph neural networks have shown advantages in modeling non-Euclidean data and structured relationships among channels or sensors in related applications [18–20], but this type of topology-aware modeling has rarely been applied to microwave breast tumor localization.

* Corresponding author: Xia Xiao (xiaxiao@tju.edu.cn).

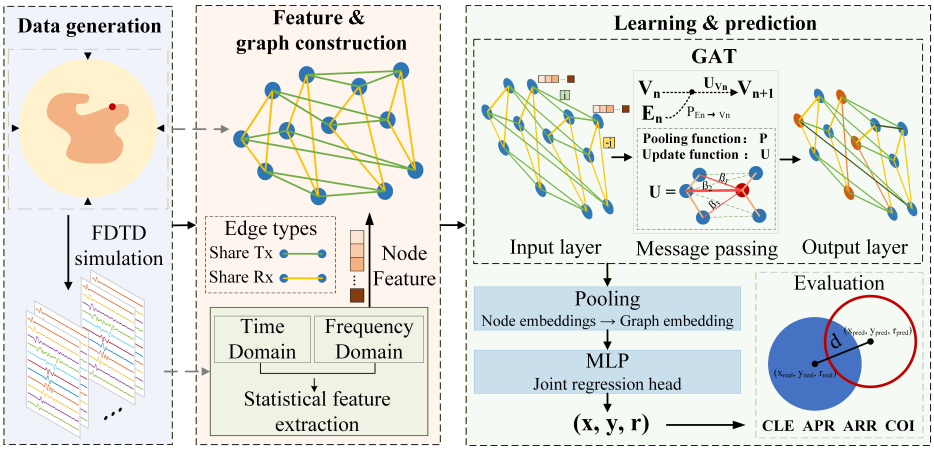

FIGURE 1. Algorithm framework for tumor localization.

Most neural networks still use backscattered signals as conventional inputs and mainly learn features from time-frequency signals, without explicitly incorporating the physical topology of antenna arrays. As a result, the structured inter-channel correlations induced by array geometry may not be fully utilized.

To address these challenges, this study proposes an edge-fusion-based graph attention network (GAT) [21]. Rather than ignoring the relationships between channels, the core of this approach is to directly encode the physical structure of the antenna array into the model architecture so that inter-channel dependencies can be learned. In terms of signal representation, this study introduces the double tree complex wavelet transform (DTCWT) for signal feature extraction and combines statistical feature selection and dimensionality reduction techniques to ensure the stability and dimensional balance of graph representation in heterogeneous breast models. Through the collaborative design of this structure and signal features, this study ultimately achieved the joint prediction of tumor spatial localization and size estimation under a unified regression architecture.

The main contributions of this work are summarized as follows:

1. The backscattered signals are reformulated as a graph, so that the physical topological relationships among Tx-Rx channels can be explicitly incorporated into the learning framework.
2. An edge-fusion-based graph attention network is introduced to adaptively capture the non-uniform importance of different measurement channels during feature aggregation.
3. A joint regression framework is developed to simultaneously estimate the tumor center coordinates and radius, enabling direct characterization of tumor location and size without image reconstruction.

2. METHOD

2.1. Overall Structure

As shown in Figure 1, the proposed framework establishes an end-to-end pipeline that directly maps multi-channel UWB backscattered signals to the tumor parameters without explicit image reconstruction. The process begins with finite-difference time-domain (FDTD) simulations to generate backscattered signals. The signals are then transformed into compact time-frequency features via dual-tree complex wavelet transform (DTCWT)-based preprocessing to reduce redundancy while preserving tumor-sensitive signatures. The Tx-Rx channels are subsequently organized into a graph, where each channel acts as a node, and the edges are defined according to the physical Tx-Rx connectivity to enable structured information exchange during learning.

The proposed architecture uses stacked GAT layers to update the node features through neighborhood message passing. Each layer in the network updates the node representations by aggregating information from adjacent nodes while incorporating the corresponding edge attributes that describe the channel relationships. Rectified linear unit (ReLU) activations were applied after each layer to introduce nonlinearity, and dropout was used during training to reduce overfitting. After the final attention layer, a global pooling operation produces a graph-level embedding, which is fed into a Multi-Layer Perceptron (MLP) regressor to predict the tumor center coordinates and equivalent radius. The network was trained with a weighted MSE loss, where the coordinate and radius terms were reweighted to account for their different numerical scales.

2.2. Dataset

In the study, four 2D numerical breast models were constructed from clinical MRI slices to represent heterogeneous tissue environments. The models followed the BI-RADS breast-density categories and were grouped by the fibroglandular tissue volume fraction. The four breast models were fatty type (Model I), scattered fibroglandular type (Model II), heterogeneously dense type (Model III), and extremely dense type (Model IV).

Figure 2 shows the four numerical breast models, where the orange, light yellow, and pink regions represent the skin, fat, and glandular tissues, respectively. A circular array of 12 uniformly spaced antennas (A1–A12) was placed along the breast boundary (black triangles). Tumors with diameters of 4–9 mm were randomly embedded within the breast region, and their

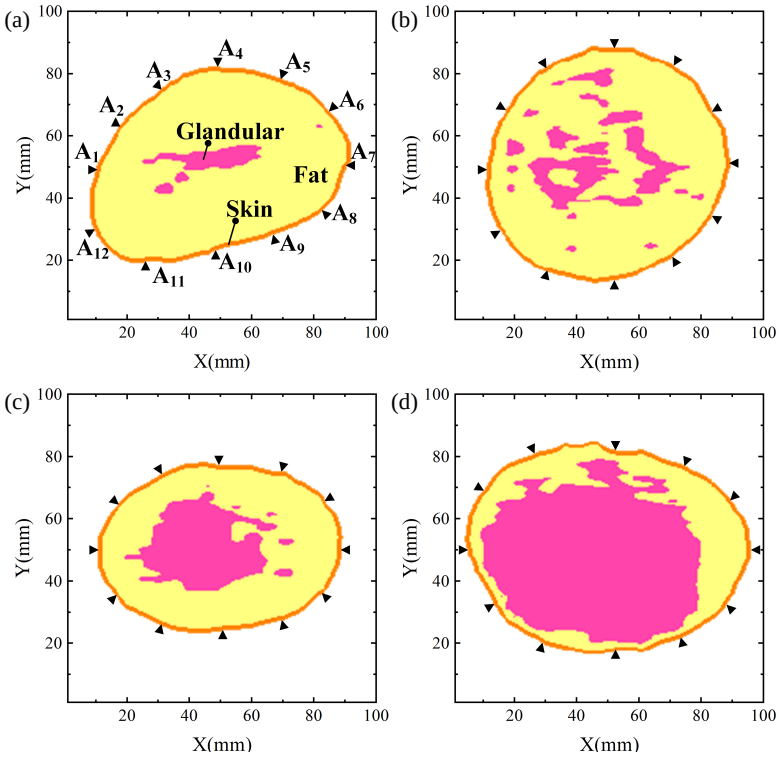

FIGURE 2. Four 2D MRI-derived breast models. (a) Model I. (b) Model II. (c) Model III. (d) Model IV.

center coordinates were randomly sampled from the admissible breast area.

Microwave scattering was simulated using the FDTD method with a spatial step size of 0.5 mm. Because breast tissue exhibits frequency dispersion in the UWB band, a single-pole Debye model was adopted to describe the complex relative permittivity $\varepsilon_{br}(\omega)$ [22]:

$$\varepsilon_{br}(\omega) = \varepsilon_{\infty} + \frac{\Delta\varepsilon}{1 + j\omega\tau} + \frac{\sigma_s}{j\omega\varepsilon_0} \tag{1}$$

where ε_{∞} is the dielectric constant at an infinite frequency; $\Delta\varepsilon$ is the difference between the static and high-frequency dielectric constants; τ is the relaxation time constant; σ_s is the static conductivity; and ε is the vacuum dielectric constant. The model parameters for each tissue type were set according to [23] and the corresponding values are summarized in Table 1.

TABLE 1. Single-pole Debye parameters for breast tissues.

	ε_{∞}	$\Delta\varepsilon$	τ (ps)	σ_s (S/m)
Skin	4.0000	33.0000	7.2300	1.1000
Fat	3.1161	1.5916	13.0000	0.0496
Glandular	12.8485	24.6430	13.0000	0.2514
Tumor	3.9000	50.1000	7.0000	0.7000

A one-transmitting-multiple-receiving (Tx-Rx) acquisition scheme was employed. A 6-GHz-centered first-derivative Gaussian pulse was used for the UWB excitation. The received signal $S(t)$ can be modeled as the additive decomposition of multiple components:

$$S(t) = S_{\text{inc}}(t) + S_{\text{skin}}(t) + S_{\text{tumor}}(t) + S_{\text{clutter}}(t) \tag{2}$$

where $S_{\text{inc}}(t)$ is the direct wave; $S_{\text{skin}}(t)$ is the skin reflection; $S_{\text{tumor}}(t)$ is the weak tumor-induced scattering; and $S_{\text{clutter}}(t)$ represents the background scattering from heterogeneous tissues. Although $S_{\text{tumor}}(t)$ is typically much weaker than the dominant components, its induced phase perturbations and envelope modulations embedded in the cluttered response provide informative cues for localization.

For each breast model, 2,000 tumor-containing samples were simulated, covering tumors with different locations and diameters. With a 12-antenna one-transmit–multiple-receive scheme, each sample comprised 132 (12×11) measurement channels, and each channel waveform contained 2,000 time points. The dataset was randomly split into training, validation, and test sets with ratios of 80%, 10% and 10% (seed $= 42$). Feature normalization parameters were computed on the training set only and then applied unchanged to the validation and test sets to avoid any information leakage. All results reported in this paper were obtained from the held-out test set.

Figure 3 shows the representative signals for Model II with antenna A1 transmitting and the remaining antennas receiving, including a no-tumor reference trace and several tumor cases with different locations and radii. Compared with the no-tumor case, the presence of a tumor introduces additional scattering components that perturb the received waveforms in specific time windows and alter their amplitude and shape. These perturbations are channel-dependent, as Tx-Rx channels that are geometrically closer to the tumor or whose propagation paths pass near the lesion exhibit more pronounced deviations from

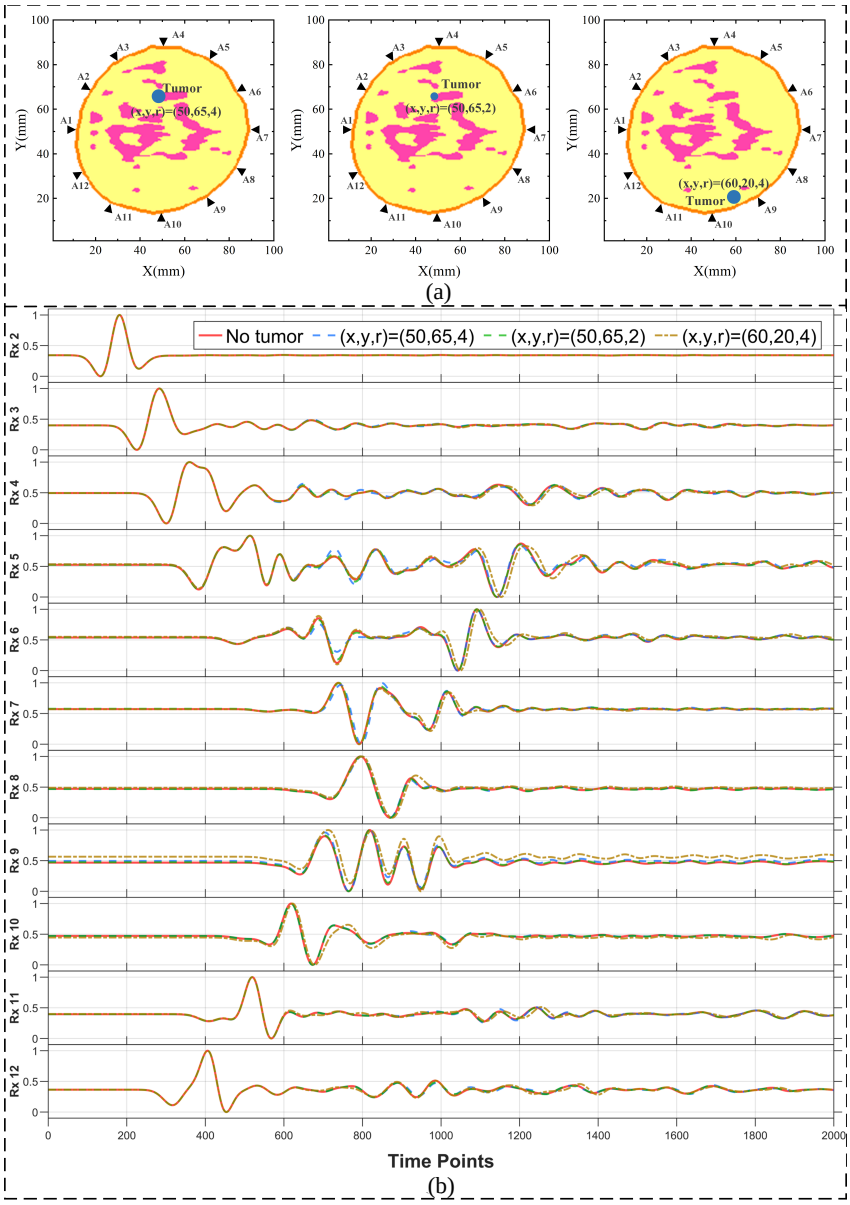

FIGURE 3. Tumor configurations and corresponding multi-channel UWB backscattered signals in Model II. (a) Representative tumor placements with different locations and radii in Model II. (b) A1-transmitted backscattered signals at A2–A12 for different tumor cases in Model II.

the reference signal. Consequently, the time positions at which differences emerge, and their relative magnitudes across receivers reflect the spatial relationship of the tumor to the antenna array and provide information for localization. For cases sharing the same location, increasing the tumor diameter consistently enlarged the deviation amplitude, indicating that the perturbation magnitude also carries information about the tumor size.

2.3. Graph Construction

In this study, a graph is an abstract relational structure rather than an image, where entities are represented as nodes and their relationships as edges [24].

This work represents the 132 Tx-Rx channels from a 12-element circular array as nodes in the graph, with signal-derived features assigned as node attributes. In GNN, nodes are the primary objects updated during message passing and feature aggregation. Therefore, treating Tx-Rx signal channels, which carry tumor-related scattering information, as nodes and defining edges through shared transmit or receive antennas is more conducive to incorporating the physical topology of the array into tumor information modeling. Given the high dimensionality and redundancy of raw microwave signals, directly feeding the original time-domain signals into the network would substantially increase the computational cost and risk of overfitting. Therefore, we applied the DTCWT to obtain multi-scale time-frequency representations [25]. Based on the energy distribution of the decomposed coefficients, five energy-dominant sub-bands were selected to preserve the principal scattering components while suppressing redundant content. For feature construction, we computed six statistical features from each se-

lected sub-band and the original time-domain signal, including energy, maximum, minimum, integral, kurtosis, and Shannon entropy. Consequently, a total of 36 (6×6) features are generated for each signal. To reduce the scale discrepancies across features and improve training stability, two-stage normalization was adopted. The first stage is feature-wise local scaling, and the second is cross-channel global normalization.

The dependencies between channels are captured by linking nodes that share the same transmitting or receiving antenna. The resulting links were treated as undirected edges in the graph. The edge attribute is encoded as a signed antenna index as follows:

$$e_{uv} = \begin{cases} +i & \text{if channels } u \text{ and } v \text{ share transmitter } A_i \\ -j, & \text{if channels } u \text{ and } v \text{ share receiver } A_j \end{cases} \quad (3)$$

where $i, j \in \{1, 2, ..., 12\}$. This encoding compactly represents both the relationship type and the corresponding antenna identity, encouraging the network to learn inter-channel dependencies consistent with the physical acquisition topology of the radar. In the implementation, e_{uv} is treated as a categorical edge feature before message passing.

2.4. Graph Attention Network with Edge-Feature Fusion

After constructing the graph topology, we employed the GAT to propagate and aggregate spatial features across the measurement channels. The network performs attention-weighted message passing, enabling it to capture nonlinear dependencies among multi-channel antenna measurements while emphasizing informative interactions.

Node features are first projected into a latent space using a multi-layer perceptron (MLP) with linear transformations and ReLU activations, mapping the 36-dimensional statistical features to higher-dimensional embeddings. To incorporate the physical relationships encoded by the graph, the edge attributes are integrated into the message-passing function, thereby linking the array topology with the learned feature space. Specifically, at the kth layer, the embedding of node v is updated as

$$h_v^{(k+1)} = \mathrm{MLP}^{(k)}\left((1+\varepsilon)\, h_v^{(k)} + \sum_{u \in N_{(v)}} \sigma\left(W^{(k)} h_u^{(k)} + B^{(k)} e_{uv}\right)\right) \quad (4)$$

where $h_v^{(k+1)}$ and $h_v^{(k)}$ denote the node embeddings at layers $k+1$ and k; $N(v)$ is the neighborhood of v; and e_{uv} is the edge attribute encoding the physical relationship between channels u and v. The nonlinearity $\sigma(\cdot)$ is set to ReLU, and the learnable parameters $W^{(k)}$, $B^{(k)}$ allow edge attributes to modulate the incoming messages, while $(1+\varepsilon)h_v^{(k)}$ provides a self-feature term to preserve node identity. Thus, node embeddings are iteratively enhanced by aggregating topology-aware edge-conditioned information from adjacent channels.

The core of the model is an adaptive attention mechanism (Figure 4) [26], which computes the attention coefficients between connected nodes and dynamically computes the attention

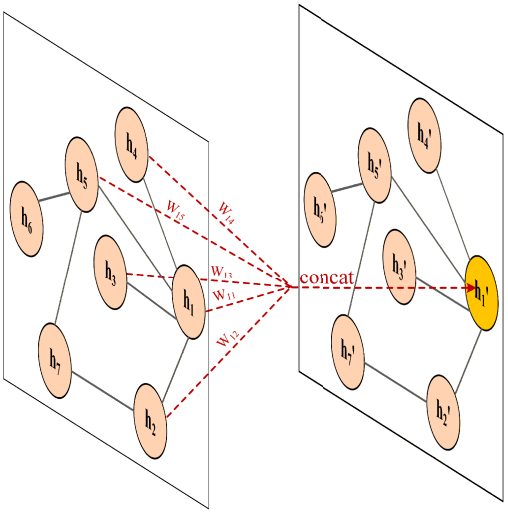

FIGURE 4. Principle of the attention mechanism.

coefficients on edges and weights messages. First, we compute an unnormalized attention score as follows:

$$S_{uv}^{(k)} = \mathrm{LeakyReLU}\left(a^{(k)\mathrm{T}}\left[W_q^{(k)} h_v^{(k)} \,\middle\|\, W_t^{(k)} h_u^{(k)} \,\middle\|\, W_e^{(k)} e_{uv}\right]\right) \quad (5)$$

where $[\cdot \,\|\, \cdot]$ denotes the concatenation; $h_v^{(k)}$ and $h_u^{(k)}$ are the node embeddings of nodes v and u, respectively; e_{uv} is the edge attribute; and $a^{(k)}$, $W_q^{(k)}$, $W_t^{(k)}$, $W_e^{(k)}$ are learnable parameters. The normalized attention coefficient is then obtained using a neighborhood-wise softmax:

$$\alpha_{uv}^{(k)} = \frac{e^{s_{uv}^{(k)}}}{\sum_{u \in N_{(v)}} e^{s_{uv}^{(k)}}} \quad (6)$$

The node update is given by:

$$h_v^{(k+1)} = \mathrm{MLP}^{(k)}\left((1+\varepsilon)\, h_v^{(k)} + \sum_{u \in N_{(v)}} \alpha_{uv}^{(k)} \sigma\left(W^{(k)} h_u^{(k)} + B^{(k)} e_{uv}\right)\right) \quad (7)$$

As shown in Figure 3, the tumor-induced scattering responses were channel-dependent. By learning attention weights during message passing, the GAT can reweight channel contributions and emphasize more informative measurements in feature aggregation.

A global pooling operation is applied after the GAT layers to obtain graph-level representations. A multi-task regression head then outputs the tumor center coordinates (x, y) and equivalent radius r. To balance the positioning accuracy and scale estimation, the comprehensive loss function LOSS was designed in this study as follows:

$$\mathrm{LOSS} = w_{xy} \times L_{xy} + w_r \times L_r \quad (8)$$

The position loss L_{xy} uses the mean square error between the predicted and real coordinates to constrain the localization

TABLE 2. Detailed configuration of the proposed network.

	Model I	Model II	Model III	Model IV
GAT depth L	3	4	3	5
Hidden dim d	128	256	128	256
Dropout	0.05	0.1	0.05	0.1
Init LR	1e-3			
Optimizer	AdamW			
LR scheduler	factor = 0.5; patience = 6/6/4/3; threshold = 5e-4; min lr = 1e-6.			
Batch /Max Epoch	64/500	64/800	64/800	64/800
Weight decay	1e-4	1e-4	1e-4	2e-4

accuracy of the model. The radius loss L_r was used to evaluate the estimation bias of the tumor size. By introducing the parameters w_{xy} and w_r, the model can effectively overcome the optimization imbalance between different dimensions and achieve synchronous characterization of tumor parameters.

2.5. Implementation Details

Separate models were trained for the four models to account for their different clutter levels and convergence behavior. We used the same data split and leakage-free normalization protocol for all experiments. The model and training-specific hyperparameters are listed in Table 2. For each model, this study selected the checkpoint with the lowest validation loss for the final evaluation on the held-out test set.

2.6. Evaluation

To comprehensively assess the model's localization performance by jointly considering position and size information, the following metrics are used:

1) Center Localization Error (CLE): CLE measures the Euclidean distance between the predicted tumor center $(x_{\text{pred}}, y_{\text{pred}})$ and the ground-truth center $(x_{\text{gt}}, y_{\text{gt}})$:

$$\text{CLE} = \sqrt{(x_{\text{pred}} - x_{\text{gt}})^2 + (y_{\text{pred}} - y_{\text{gt}})^2} \tag{9}$$

2) Area Recall Ratio (ARR): A_{gt} and A_{p} denote the ground-truth and predicted regions, respectively. The ARR quantifies the fraction of the ground-truth area covered by the prediction as follows:

$$\text{ARR} = \frac{|A_{\text{gt}} \bigcap A_{\text{p}}|}{|A_{\text{gt}}|} \tag{10}$$

An ARR approaching 1 signified fewer missed ground-truth regions. Since the predicted tumor size directly affects the covered area, ARR is sensitive not only to positional deviation but also to the underestimation of the tumor radius.

3) Area Precision Ratio (APR): The APR quantifies the fraction of the predicted area that overlaps with the ground truth.

$$\text{APR} = \frac{|A_{\text{gt}} \bigcap A_{\text{p}}|}{|A_{\text{p}}|} \tag{11}$$

A higher APR value indicates more compact and accurate predictions. An overestimated radius enlarges the predicted region and may include excessive non-tumor area.

4) Comprehensive Overlap Index (COI): To strike a balance between detection coverage and spatial specificity, the COI is defined as the harmonic mean of ARR and APR:

$$\text{COI} = 2 \times \frac{\text{ARR} \times \text{APR}}{\text{ARR} + \text{APR}} \tag{12}$$

COI provides a balanced overlap-based evaluation by penalizing both insufficient coverage and excessive over-prediction.

3. RESULT

3.1. Performance

Figure 5 shows the representative localization results for 20 randomly selected test samples from each of the four breast-model categories. The red-filled circles denote the ground-truth tumors, whereas the blue circles indicate the tumor boundaries predicted by the proposed model. Across tissue backgrounds with varying densities, the predicted area showed a significant spatial overlap with the ground truth, indicating that the proposed method can effectively predict the tumor location and size.

To further quantify the performance, Table 3 summarizes the statistical results for the four breast models, reflecting both average accuracy and variability. The mean CLE remained below 2.5 mm for all the models. Model I achieved the best performance (0.99 ± 0.65 mm). As the glandular content increased, extracting tumor-related features from heterogeneous scattering responses became increasingly difficult, leading to a decrease in prediction accuracy. However, Model II showed a higher error than Model III. This phenomenon may be related to the stronger structural non-uniformity and increased interface-induced scattering in Model II.

Figure 6 illustrates the distributions of CLE and COI across the four breast models. Compared with Table 3, it provides additional information on distribution shape, dispersion, and outliers. Smaller CLE indicates more accurate tumor-center localization, whereas larger COI indicates better spatial overlap between the predicted and ground-truth tumor regions. In

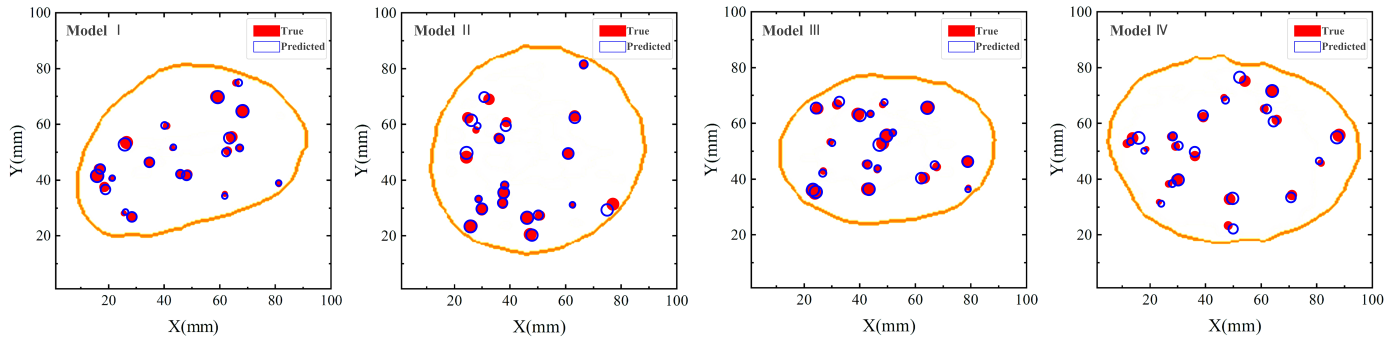

FIGURE 5. Predicted and ground-truth tumors across the four breast models.

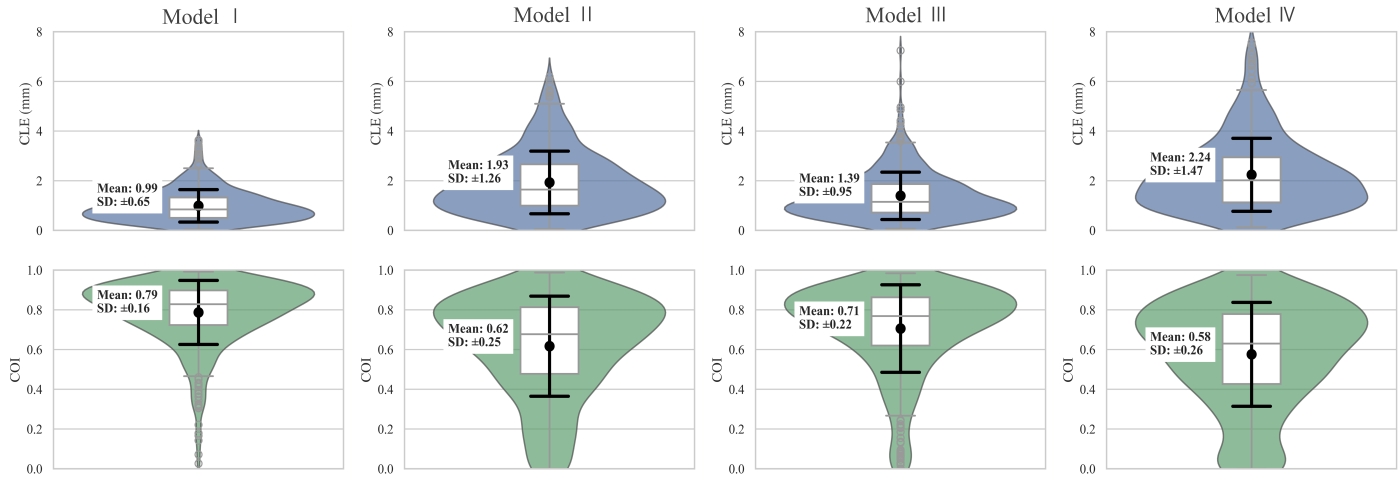

FIGURE 6. Distributions of CLE and COI across the four breast models.

TABLE 3. Performance of the proposed method on four breast models (mean ± standard deviation).

	CLE (mm)	ARR (%)	APR (%)	COI (%)
Model I	0.99 ± 0.65	78.78 ± 16.25	78.64 ± 16.11	78.68 ± 16.12
Model II	1.93 ± 1.26	61.79 ± 25.54	61.86 ± 25.23	61.68 ± 25.19
Model III	1.39 ± 0.95	70.28 ± 22.30	71.03 ± 22.07	70.57 ± 22.04
Model IV	2.24 ± 1.47	57.54 ± 26.29	57.84 ± 26.30	57.57 ± 26.14

TABLE 4. CLE and COI under different tumor diameters across the four breast models.

	4 mm–5 mm		6 mm–7 mm		8 mm–9 mm	
	CLE (mm)	COI (%)	CLE (mm)	COI (%)	CLE (mm)	COI (%)
Model I	1.01	70.66	0.92	81.97	0.97	85.46
Model II	2.14	45.59	1.87	64.36	1.79	73.01
Model III	1.65	55.90	1.26	75.27	1.25	81.34
Model IV	2.57	40.67	2.11	59.88	2.10	68.95

this work, we regard COI values above 0.5 as indicating a reasonable overlap. Although the glandular structure becomes progressively more complex from Model I to Model IV, both CLE and COI distributions remain relatively concentrated in favorable ranges across models, suggesting that the proposed GAT framework delivers consistent performance under heterogeneous tissue backgrounds.

We further analyzed the effect of tumor diameter and the effect of noise on the prediction performance. As shown in Table 4, CLE increased, and COI decreased as the tumor diameter became smaller. For smaller tumors, the scattered field

TABLE 5. Performance of the proposed method on four breast models (mean ± standard deviation).

SNR	Model	CLE (mm)	ARR (%)	APR (%)	COI (%)
10	I	1.90 ± 1.04	60.94 ± 22.90	60.75 ± 23.10	60.77 ± 22.88
10	II	2.63 ± 1.29	49.88 ± 24.60	48.91 ± 24.02	49.07 ± 23.79
10	III	2.41 ± 1.32	53.57 ± 26.64	52.67 ± 26.43	53.00 ± 26.34
10	IV	2.74 ± 1.84	49.43 ± 29.79	50.54 ± 30.46	49.86 ± 30.05
20	I	1.47 ± 0.74	68.78 ± 19.35	68.01 ± 19.28	68.36 ± 19.25
20	II	2.17 ± 1.14	56.58 ± 23.80	56.79 ± 24.01	56.55 ± 23.66
20	III	1.70 ± 0.94	64.11 ± 22.83	64.87 ± 23.17	64.45 ± 22.95
20	IV	2.40 ± 1.69	53.62 ± 28.86	53.85 ± 29.50	53.16 ± 29.08

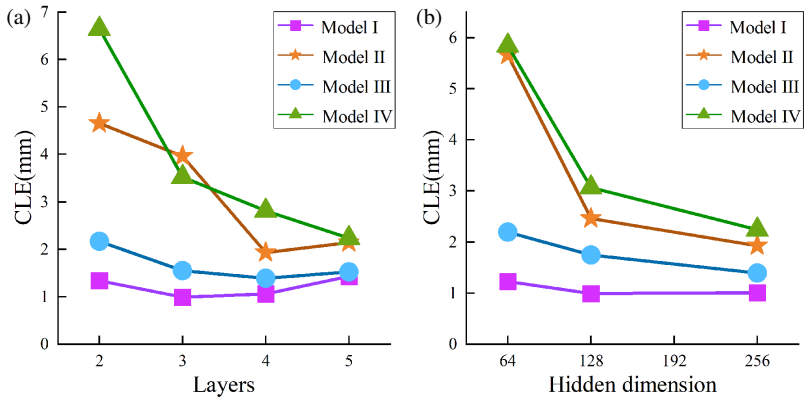

FIGURE 7. Effect of the number of GAT layers and hidden dimension on localization accuracy.

intensity is weaker, making tumor-related signatures more susceptible to being masked by the background clutter and skin-reflection components. Table 5 shows that noise also degrades performance. Compared with the noise-free case, CLE increased while COI decreased under both 20 dB and 10 dB conditions, with more severe degradation at 10 dB. These findings indicate that both smaller tumor size and stronger noise reduce the discriminability of tumor-related features and thus increase localization difficulty.

3.2. Influence of GNN Hyperparameters on Prediction Performance

Network depth determines the extent of message passing and the effective receptive field on the graph. Increasing the number of layers allows the model to aggregate information from multi-hop neighbors, potentially capturing higher-order dependencies among measurement channels. As shown in Figure 7, a two-layer network provides limited propagation, resulting in larger errors and signs of underfitting. Performance improves as depth increases: Models I and III achieve their best results at approximately three layers. However, further increasing depth yields diminishing returns and may degrade performance, likely due to redundant aggregation and overfitting. In contrast, more heterogeneous Models II and IV benefit from deeper architectures (around four and five layers, respectively), suggesting that more complex tissue backgrounds may require additional propagation hops to effectively integrate informative inter-channel cues.

Increasing the hidden dimension from 64 to 128 yielded a clear performance improvement, particularly for dense models, where weak tumor signatures must be separated from strong clutter. When further increased to 256, the gain saturates for Model I, whereas the higher-density models still show marginal improvement. Overall, these results indicate that more complex tissue backgrounds benefit from a larger representational capacity.

4. DISCUSSION

The proposed GAT framework demonstrated clear advantages for tumor localization in heterogeneous breast tissues. As summarized in Table 3, it achieved stable performance across four heterogeneous 2D breast models, with mean CLEs of 0.99, 1.93, 1.39, and 2.24 mm and mean COIs of 78.68%, 61.68%, 70.57%, and 57.57%, respectively.

Table 6 summarizes the comparisons between this study and other studies. Compared with the probability-map-based deep learning method in [16], which generates pixel-wise tumor probability maps and reports a mean center error of 1.2 ± 0.9 cm together with image-level similarity metrics, the present work directly regresses tumor center coordinates and equivalent radius as explicit physical parameters, enabling a more direct and physically interpretable assessment of the predicted tumor region. Compared with the wavelet-based GA-NN approach in [27], which reports mean localization errors of 0.6076, 3.0813, 2.0798, and 3.2988 mm on four heterogeneous breast models, our method maintains consistently sub-3-mm local-

TABLE 6. Comparison with the other microwave breast tumor localization works.

Ref.	Method	Dataset acquisition	Performance
[16]	Deep learning-based tumor spatial localization by probability maps	1. Four heterogeneous 2D breast models. 2. Method of moments	Classification accuracy: 98.4%; mean center error: 1.2 ± 0.9 cm; Soft-Dice: 0.144 ± 0.078; NCC: 0.337 ± 0.148; NRMSE: 0.809 ± 0.057.
[27]	Wavelet-based feature extraction and Genetic Algorithm-Neural Network	1. Four heterogeneous 2D breast models. 2. Finite-difference time-domain simulation.	Mean localization error for four models: 0.6076, 3.0813, 2.0798, 3.2988 mm.
[28]	Convolutional Neural Network	3. Simplified 2D homogeneous background with two circular inclusions. 4. Method of moments	Example-wise errors (2 samples): center and radius errors 2.02–3.59%
This work	Graph Attention Network	1. Four heterogeneous 2D breast models. 2. Finite-difference time-domain simulation.	1. Mean CLE (mm) for four models, respectively: 0.9876, 1.9288, 1.3910, 2.2380 mm; 2. Mean COI (%) for four models, respectively: 78.68, 61.68, 70.57, 57.57.

ization and additionally provides overlap-based evaluation that jointly reflect localization and sizing quality. In contrast, the CNN-based method in [28] considers a simplified 2D homogeneous scattering scenario and reports example-wise relative errors (%). These results indicate that explicitly representing the antenna-array topology as a graph and applying attention-based message passing can better exploit non-Euclidean inter-channel dependencies in complex scattering media, enabling accurate mapping from multi-channel backscattered signals to tumor location and size.

All the calculations are performed on a 14-core CPU, a 16 GB RAM, and an RTX 4060 GPU, with most calculations accelerated by the GPU. A complete training required about 45 minutes, and the process of searching for the optimal hyperparameters took over 3 hours. For a trained network, breast tumor localization required only about 1 s, indicating relatively high inference efficiency. Through algorithm parallelization, hardware upgrades, and potential hardware implementation, the consumed time is expected to be reduced.

Although the proposed framework achieved promising results, several limitations remain. The present study is based on 2D simulation models and only validates the feasibility of the algorithm under controlled conditions, which cannot fully reflect the complexity of real measurement environments. Extending the framework to 3D breast tumor localization will involve more complex electromagnetic propagation and scattering, thereby increasing the cost of data generation and model training. The antenna configuration will also need to be adjusted accordingly. In the current study, a uniformly distributed 12-antenna circular array was adopted to provide full coverage of the breast region under 2D conditions while maintaining geometric consistency among Tx-Rx channels. For future 3D scenarios, vertically staggered multi-layer antenna arrangements will be considered to improve coverage at different depths. A denser and more uniform array may also help suppress strong skin reflections during post-processing. Based on related studies, we preliminarily consider a two-layer structure with eight antennas per layer, although the optimal sensor number and arrangement still require further investigation under 3D models, hardware constraints, and practical measurement conditions. Translation to clinical applications remains challenging. More realistic breast models, more complex tumor morphologies, and richer tissue heterogeneity need to be incorporated. In addition, practical factors such as measurement noise, antenna mismatch, and positioning errors may affect signal distributions and model generalization.

Future work will therefore consider coupling media to improve antenna performance, optimize the model structure, and combine skin-reflection suppression algorithms with the proposed network for 3D validation and experimental verification.

5. CONCLUSION

This study proposes a microwave breast tumor localization framework based on a graph attention network (GAT). By constructing a topology-aware graph that encodes inter-channel relationships, the framework directly regresses the tumor geometric parameters from UWB backscattered signals, bypassing computationally expensive image reconstruction. Across four heterogeneous 2D breast-model categories, the proposed method achieved mean center localization errors (CLE) of 0.99 mm, 1.93 mm, 1.39 mm, and 2.24 mm, respectively, while the mean Comprehensive Overlap Index (COI) exceeded 0.50 for all categories. These results suggest that topology-aware graph representation and attention-based aggregation can effectively exploit non-Euclidean inter-channel dependencies and improve the joint localization-and-sizing performance under highly heterogeneous tissue conditions. In future work, we will extend the framework to three-dimensional models and validate it using clinical or measurement-based datasets.

ACKNOWLEDGEMENT

The authors are grateful to the National Key Research and Development Program of China (Grant No. 2025YFC2423102).

REFERENCES

[1] Bray, F., M. Laversanne, H. Sung, J. Ferlay, R. L. Siegel, I. Soerjomataram, and A. Jemal, "Global cancer statistics 2022: GLOBOCAN estimates of incidence and mortality worldwide for 36 cancers in 185 countries," *CA: A Cancer Journal for Clinicians*, Vol. 74, No. 3, 229–263, 2024.

[2] Hwang, E. S., D. Y. Lichtensztajn, S. L. Gomez, B. Fowble, and C. A. Clarke, "Survival after lumpectomy and mastectomy for early stage invasive breast cancer: The effect of age and hormone receptor status," *Cancer*, Vol. 119, No. 7, 1402–1411, 2013.

[3] Giaquinto, A. N., H. Sung, K. D. Miller, J. L. Kramer, L. A. Newman, A. Minihan, A. Jemal, and R. L. Siegel, "Breast cancer statistics, 2022," *CA: A Cancer Journal for Clinicians*, Vol. 72, No. 6, 524–541, 2022.

[4] Lazebnik, M., D. Popovic, L. McCartney, C. B. Watkins, M. J. Lindstrom, J. Harter, S. Sewall, T. Ogilvie, A. Magliocco, T. M. Breslin, *et al.*, "A large-scale study of the ultrawideband microwave dielectric properties of normal, benign and malignant breast tissues obtained from cancer surgeries," *Physics in Medicine & Biology*, Vol. 52, No. 20, 6093–6115, 2007.

[5] Lu, M., X. Xiao, Y. Pang, G. Liu, and H. Lu, "Detection and localization of breast cancer using UWB microwave technology and CNN-LSTM framework," *IEEE Transactions on Microwave Theory and Techniques*, Vol. 70, No. 11, 5085–5094, Nov. 2022.

[6] Hagness, S. C., A. Taflove, and J. E. Bridges, "Two-dimensional FDTD analysis of a pulsed microwave confocal system for breast cancer detection: Fixed-focus and antenna-array sensors," *IEEE Transactions on Biomedical Engineering*, Vol. 45, No. 12, 1470–1479, 1998.

[7] Lim, H. B., N. T. T. Nhung, E.-P. Li, and N. D. Thang, "Confocal microwave imaging for breast cancer detection: Delay-multiply-and-sum image reconstruction algorithm," *IEEE Transactions on Biomedical Engineering*, Vol. 55, No. 6, 1697–1704, Jun. 2008.

[8] Miao, Z. and P. Kosmas, "Multiple-frequency DBIM-TwIST algorithm for microwave breast imaging," *IEEE Transactions on Antennas and Propagation*, Vol. 65, No. 5, 2507–2516, 2017.

[9] Awasthi, S. and P. Jain, "The application of a novel clutter removal algorithm to SAR beamforming in breast microwave imaging," *Biomedical Signal Processing and Control*, Vol. 100, 107017, 2025.

[10] Wang, J., M. Zhang, Y. Bai, H. Xu, and Y. Fan, "Distance compensation-based dual adaptive artifact removal algorithm in microwave breast tumor imaging system," *Biomedical Signal Processing and Control*, Vol. 88, 105598, 2024.

[11] Karam, S. A. S., D. O'Loughlin, and B. M. Asl, "A novel sophisticated form of DMAS beamformer: Application to breast cancer detection," *Biomedical Signal Processing and Control*, Vol. 74, 103516, 2022.

[12] Franceschini, S., M. M. Autorino, M. Ambrosanio, V. Pascazio, and F. Baselice, "A deep learning approach for diagnosis support in breast cancer microwave tomography," *Diagnostics*, Vol. 13, No. 10, 1693, 2023.

[13] Zardi, F., L. Tosi, M. Salucci, and A. Massa, "A physics-driven AI approach for microwave imaging of breast tumors," *IEEE Transactions on Antennas and Propagation*, Vol. 73, No. 7, 4661–4676, Jul. 2025.

[14] Liu, G., X. Xiao, H. Song, and T. Kikkawa, "Precise detection of early breast tumor using a novel EEMD-based feature extraction approach by UWB microwave," *Medical & Biological Engineering & Computing*, Vol. 59, No. 3, 721–731, 2021.

[15] Conceição, R. C., H. Medeiros, D. M. Godinho, M. O'Halloran, D. Rodriguez-Herrera, D. Flores-Tapia, and S. Pistorius, "Classification of breast tumor models with a prototype microwave imaging system," *Medical Physics*, Vol. 47, No. 4, 1860–1870, 2020.

[16] Borghouts, M., M. Ambrosanio, S. Franceschini, M. M. Autorino, V. Pascazio, and F. Baselice, "Microwave breast sensing via deep learning for tumor spatial localization by probability maps," *Bioengineering*, Vol. 10, No. 10, 1153, 2023.

[17] Rana, S. P., M. Dey, R. Loretoni, M. Duranti, M. Ghavami, S. Dudley, and G. Tiberi, "Radiation-free microwave technology for breast lesion detection using supervised machine learning model," *Tomography*, Vol. 9, No. 1, 105–129, Jan. 2023.

[18] Wang, C., Y. Wang, P. Ding, S. Li, X. Yu, and B. Yu, "ML-FGAT: Identification of multi-label protein subcellular localization by interpretable graph attention networks and feature-generative adversarial networks," *Computers in Biology and Medicine*, Vol. 170, 107944, 2024.

[19] Tian, Y., H. Chen, C. Xu, and Y. Wang, "Image processing GNN: Breaking rigidity in super-resolution," in *2024 IEEE/CVF Conference on Computer Vision and Pattern Recognition (CVPR)*, 24 108–24 117, Seattle, WA, USA, 2024.

[20] Yu, H., C. She, Y. Hu, G. Wang, R. Wang, B. Vucetic, and Y. Li, "Floor-plan-aided indoor localization: Zero-shot learning framework, data sets, and prototype," *IEEE Journal on Selected Areas in Communications*, Vol. 42, No. 9, 2472–2486, Sep. 2024.

[21] Vrahatis, A. G., K. Lazaros, and S. Kotsiantis, "Graph attention networks: A comprehensive review of methods and applications," *Future Internet*, Vol. 16, No. 9, 318, 2024.

[22] Lazebnik, M., M. Okoniewski, J. H. Booske, and S. C. Hagness, "Highly accurate Debye models for normal and malignant breast tissue dielectric properties at microwave frequencies," *IEEE Microwave and Wireless Components Letters*, Vol. 17, No. 12, 822–824, 2007.

[23] Zastrow, E., S. K. Davis, M. Lazebnik, F. Kelcz, B. D. Van Veen, and S. C. Hagness, "Development of anatomically realistic numerical breast phantoms with accurate dielectric properties for modeling microwave interactions with the human breast," *IEEE Transactions on Biomedical Engineering*, Vol. 55, No. 12, 2792–2800, 2008.

[24] Scarselli, F., M. Gori, A. C. Tsoi, M. Hagenbuchner, and G. Monfardini, "The graph neural network model," *IEEE Transactions on Neural Networks*, Vol. 20, No. 1, 61–80, Jan. 2009.

[25] Kingsbury, N., "The dual-tree complex wavelet transform: A new efficient tool for image restoration and enhancement," in *9th European Signal Processing Conference (EUSIPCO 1998)*, 1–4, Rhodes, Greece, 1998.

[26] Veličković, P., G. Cucurull, A. Casanova, A. Romero, P. Liò, and Y. Bengio, "Graph attention networks," *arXiv preprint arXiv:1710.10903*, 2017.

[27] Lu, M., X. Xiao, G. Liu, and H. Lu, "Microwave breast tumor localization using wavelet feature extraction and genetic algorithm-neural network," *Medical Physics*, Vol. 48, No. 10, 6080–6093, 2021.

[28] Bayat, I. H., I. Akduman, and S. Doğu, "Convolutional neural network for joint detection and material classification of breast tumors," in *2025 9th International Symposium on Innovative Approaches in Smart Technologies (ISAS)*, 1–4, Gaziantep, Turkiye, 2025.